

Article

Furfural Analogs as Sustainable Corrosion Inhibitors—Predictive Efficiency Using DFT and Monte Carlo Simulations on the Cu(111), Fe(110), Al(111) and Sn(111) Surfaces in Acid Media

Hassan Bourzi ¹, Rachid Oukhrib ¹ , Brahim El Ibrahimi ¹, Hicham Abou Oualid ² ,
Youness Abdellaoui ³ , Bouchra Balkard ¹, Souad El Issami ¹, Mustapha Hilali ¹, Lahcen Bazzi ¹
and Christophe Len ^{4,5,*}

¹ Apply Chemistry-Physic Team, Faculty of Sciences, Ibn Zohr University, 80000 Agadir, Morocco; h.bourzi@gmail.com (H.B.); rachid.oukhrb1@gmail.com (R.O.); brahimhm@gmail.com (B.E.I.); bouchra.balkard@gmail.com (B.B.); s.elissami19@gmail.com (S.E.I.); hilali.mustapha@gmail.com (M.H.); lahcn_bazzi@yahoo.fr (L.B.)

² Laboratory of Biotechnology, Materials and Environment, Faculty of Sciences, Ibn Zohr University, 80000 Agadir, Morocco; h.abououalid@gmail.com

³ Facultad de Ingeniería, Universidad Autónoma de Yucatán, Av. Industrias no Contaminantes por Periférico Norte Apartado Postal 150 Cordemex, 97310 Mérida, Mexico; abdellaoui.youness@gmail.com

⁴ Institute of Chemistry for Life and Health Sciences, CNRS, Chimie ParisTech, PSL Research University, 11 rue Pierre et Marie Curie, F-75005 Paris, France

⁵ Sorbonne Universités, Université de Technologie de Compiègne, Centre de Recherche Royallieu, CS 60 319, F-60203 Compiègne CEDEX, France

* Correspondence: christophe.len@chimieparistech.psl.eu

Received: 6 March 2020; Accepted: 13 April 2020; Published: 18 April 2020



Abstract: Nowadays, theoretical calculation tools have become powerful in predicting the behavior of corrosion inhibitors on the surface of metals and, therefore, avoiding energy consumption and the cost of experimental tests. This work aims to predict the inhibitory power of some furan derivatives on Cu (111), Fe (110), Al (111) and Sn (111) surfaces in acidic media. For this purpose, three furan derivatives—furan-2-carbaldehyde (FF1), 5-(hydroxymethyl)furfural (FF2) and 5-(hydroxymethyl)furoic acid (FF3)—have been selected to compare their intrinsic properties against corrosion as well as their behavior on iron (Fe), copper (Cu), aluminum (Al) and tin (Sn) surfaces in acid medium. Typically, the anti-corrosive properties of FF1, FF2 and FF3 were studied by using quantum chemical calculations and Monte Carlo simulations. Density Functional Theory (DFT), lowest unoccupied (E_{LUMO}) and highest occupied (E_{HOMO}) molecular orbital energies, energy gap (ΔE), chemical hardness (η), softness (σ), electronegativity (χ), electrophilicity (ω) and nucleophilicity (ε) have been calculated and discussed. Theoretical vibrational spectra were also calculated to exhibit the functional groups in the selected chemicals. On the other hand, the adsorption behaviors of FF1, FF2 and FF3 were studied on the Fe(110), Cu(111), Al(111) and Sn(111) surfaces. As a result, the adsorption energies of all molecules are ordered as Fe(110) < Cu(111) < Al(111) < Sn(111) and FF3 seems to be more effective as a corrosion inhibitor due to the existence of both carboxylic acid and hydroxyl groups, which consist of favorable sites of adsorption into the metal surface.

Keywords: furan derivatives; corrosion; DFT; adsorption behavior; metal surface; prediction; Monte Carlo simulations

1. Introduction

Corrosion still has a huge economic impact in most industrial countries today, accounting for about 3–4 percentage points of the gross domestic product (GDP) [1–3]. As fossil resources are being depleted at a rapid rate, there is an urgent need to develop renewable energies to replace fossil fuels derived from oil. Biomass, the only renewable resource of organic carbon in nature, is a response to oil substitution [1,2]. However, the management of corrosion in biorefinery complexes has only recently been identified as a potential challenge in the scientific literature [4]. From an industrial point of view, the effects related to corrosion must be anticipated in order to apprehend an appropriate evaluation of the possibilities of Capital Expenditure (CAPEX) and Operational Expenditure (OPEX), return on investment and extension of the life of the installations. Indeed, the aging, maintenance and modernization operations of biorefineries can induce new potential corrosive environments that must be identified and reassessed regularly. Operational disruptions, extra costs, industrial risks and environmental impacts can be effective due to the erroneous or underestimated evaluation of corrosion issues. Several studies have evaluated the annual direct cost of corrosion to be about 3.1% of gross national product (GNP) in industrialized countries [1–3].

As a preventive method to protect the material from corrosion [5–8], green-extracted natural products [5,9–11] and small organic chemicals [12–16] have shown good properties. Compounds having heterocyclic and aromatic cores, having heterogeneous atoms such as oxygen, nitrogen and sulfur atoms, are widely used due to π and heterogeneous atom interactions with the surface of the metal [17–22]. Among the chemicals having this structure, the biobased platform molecule furfural [23–32] is a potential candidate for the treatment of corrosion.

Currently, computational software is becoming a much-used and trusted tool to explain the behavior of corrosion inhibitors in several media and metal surfaces [6,33–36]. Density functional theory (DFT) is a computational modeling method usually used to investigate the intrinsic properties of molecules. For inhibitors, it is mainly conducted to predict chemical properties such as the highest occupied molecular orbital–lowest unoccupied molecular orbital (HOMO–LUMO) energy gap, chemical hardness, softness, electronegativity, chemical potential, proton affinity, electrophilicity and nucleophilicity of chemical species. On the other hand, Monte Carlo simulations were used to understand the behavior of inhibitors on the metal surfaces. Indeed, adsorption energy and binding energy are calculated and investigated [37–45]. To the best of our knowledge, furanic derivatives were studied using theoretical tools only for conversion [46,47], electrochemical oxidation [48] and hydrodeoxygenation [49,50]. In our work, theoretical studies were investigated to predict the efficiency of three selected furan derivatives: furan-2-carbaldehyde (FF1), 5-(hydroxymethyl) furfural (FF2) and 5-(hydroxymethyl)furoic acid (FF3). Firstly, the intrinsic properties such as the $E_{\text{HOMO}}-E_{\text{LUMO}}$ energy gap (ΔE), chemical hardness (η), electronegativity (χ), the fraction of electrons transferred (ΔN), total negative charges and dipole moment of FF1, FF2 and FF3 were studied by using quantum chemical calculations. On the other hand, the adsorption and binding energies of these three molecules were examined on the surface of several metals, namely Cu(111), Fe(110), Al(111) and Sn(111) using Monte Carlo simulations.

2. Computational Details

2.1. DFT Calculations

Employing the Gaussian 03W program package, the density functional theory (DFT) calculations were performed on the studied furfurals derivatives FF1, FF2 and FF3 in gas and aqueous phases. All molecules were geometrically optimized using the DFT/B3LYP method associated with 6-31G++(2d,p) basis sets, which is widely used in the investigation of organic corrosion inhibitors [51,52]. The absence of imaginary vibration frequencies confirmed the optimization process. Afterward, several relevant molecular electronic structure parameters (global and local indicators) were calculated. There include the lowest unoccupied (E_{LUMO}) and highest occupied (E_{HOMO}) molecular orbital energies, as well as

gap energy (ΔE , Equation (1)), electronegativity (χ , Equation (2)), hardness (η , Equation (3)), fraction of electrons transferred (ΔN , Equation (4)), electrophilicity (ω), nucleophilicity (ϵ) and dipole moment (μ) [53]. Furthermore, the frontier molecular orbitals (i.e., HOMO and LUMO) repartitions and 2D electrostatic potential plots of each furfural derivative were calculated and figured.

$$\Delta E = E_{\text{LUMO}} - E_{\text{HOMO}} \quad (1)$$

$$\chi = -\frac{1}{2}(E_{\text{LUMO}} + E_{\text{HOMO}}) \quad (2)$$

$$\eta = \frac{1}{2}(E_{\text{LUMO}} - E_{\text{HOMO}}) \quad (3)$$

$$\Delta N = \frac{\phi - \chi}{2 \times \eta} \quad (4)$$

where ϕ is the work function of metal surface ($\phi_{\text{Cu}} = 4.94$ eV, $\phi_{\text{Fe}} = 4.82$ eV, $\phi_{\text{Al}} = 4.26$ eV and $\phi_{\text{Sn}} = 4.42$ eV) [54–56].

2.2. Monte Carlo Simulations

In the recent years, Monte Carlo simulations have become a potent computation tool that is employed widely to examine the possible inhibitor–metal interactions for a large number of inhibition systems [41,57]. For this purpose, the interaction between the investigated furfural compounds and selected metal surfaces (Cu, Fe, Al and Sn) was studied using Monte Carlo simulations, as the temperature of the system was slowly decreased (i.e., simulated annealing algorithm [58,59]). The organic inhibitors are widely used in the acidic environment, which is considered in the current study. In such an environment, the surface of the selected substrates consists of pure metal [60]. To predict the most adequate (h k l) Miller index of each metal surface for constructing of simulation box, the Bravais–Friedel–Donnay–Harker (BFDH) method was utilized [53]. Five layers and a vacuum region of 60 Å were used to model the slab of each studied metal in the current work. The Van der Waals and electrostatic interactions were calculated via the atom-based and Ewald summation methods, respectively. Materials Studio 6.0 software was utilized to perform these calculations with the Condensed-phase Optimized Molecular Potentials for Atomistic Simulation Studies (COMPASS) force field. These simulations were carried out using five heating ramps with 50,000 steps each. The obtained conformers were pre-geometrized and inputted with a temperature range between 100 and 10⁵ K. To get results with excellent quality, the convergence threshold was fixed at 5 × 10^{−5} Å, 5 × 10^{−3} kcal mol^{−1} Å^{−1} and 10^{−4} kcal mol^{−1} for displacement, force and energy, respectively. The charges used in the calculation were given by the employed force field. The adsorption energy (E_{ads}) of the furfural derivative on each metal surface type was calculated according to the following expression [8]:

$$E_{\text{ads}} = E_{\text{T}} - (E_{\text{Surf}} + E_{\text{ads}}^{\text{Furfural}}) \quad (5)$$

where E_{T} denotes the total energy of the whole system, E_{Surf} is the energy of the metal surface and $E_{\text{ads}}^{\text{Furfural}}$ is the energy of the adsorbed furfural derivative on metal surface.

In the present work, we have limited the simulations process in the gas phase to reduce the required time for calculations. Additionally, it was reported [61,62] that the aqueous phase can influence the magnitude of calculated adsorption energies of inhibitor molecules, while the trend of these energies remains the same one either with or without solvent.

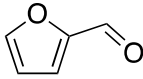
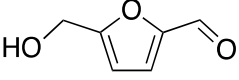
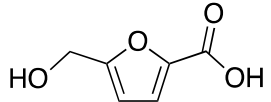
3. DFT Performances

3.1. Optimized Structures

The furfural derivatives FF1, FF2 and FF3 contain several functional groups such as formyl, hydroxyl and carboxylic groups (Table 1). The optimized structures of inhibitor molecules in aqueous

and gas phases using the hybrid DFT functional method (i.e., B3LYP/6-31G++(2d,p)) are shown in Figures 1 and 2, respectively.

Table 1. Chemical details of FF1, FF2 and FF3 furan derivatives.

Notation	Structure/Name	Function
FF1	 furan-2-carbaldehyde	Aldehyde
FF2	 5-(hydroxymethyl)furfural	Aldehyde Alcohol
FF3	 5-(hydroxymethyl)furoic acid	Carboxylic acid Alcohol

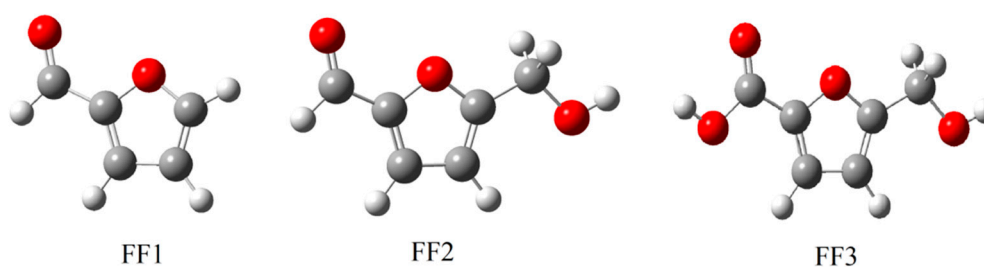


Figure 1. The optimized structures of inhibitor molecules in the gas phase using the DFT/B3LYP/6-31++G(2d,p) method. DFT: Density Functional Theory.

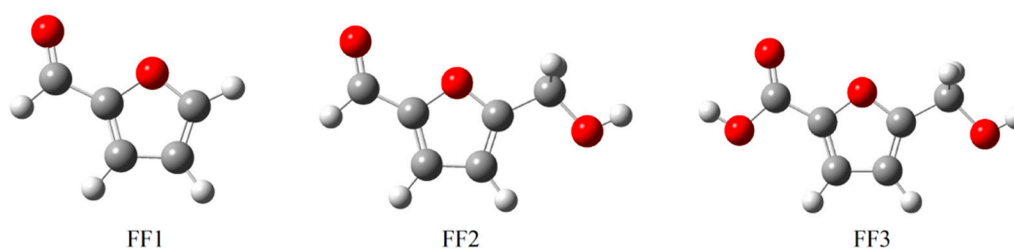


Figure 2. The optimized structures of inhibitor molecules in the aqueous phase using the DFT/B3LYP/6-31++G(2d,p) method.

In order to highlight the functional groups in FF1, FF2 and FF3, the vibrational spectroscopy of all molecules was calculated using the B3LYP/6-31++G(2d,p) method (Figure 3). The vibrational spectra of FF1, FF2 and FF3 confirmed the existence of aldehyde, aldehyde and alcohol and carboxylic acid and alcohol, respectively. The peaks at around 3000 cm^{-1} are mainly attributed to hydroxyl groups. Moreover, the peaks at 1705 , 1698 and 1745 cm^{-1} are attributed to carbonyl groups.

Before launching the other theoretical calculations, the structure optimization step of the investigated molecules was done in aqueous and gas phases to determine the geometrical structure with a local minimum on the conformational. Namely, the precise theoretical determination of the geometry of FF1, FF2 and FF3 chemicals were studied at the minima of their potential energy [33]. Thus, it is essential to obtain optimized structures of studied inhibitors to subsequently determine the other parameters, such as a map of electrostatic potential (ESP).

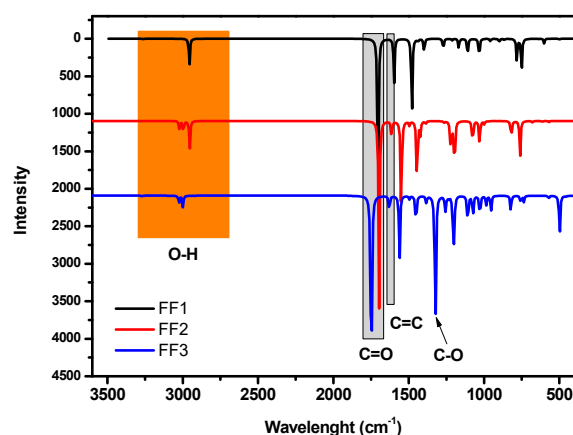


Figure 3. Vibrational spectra of FF1, FF2 and FF3 in the range of 400 to 4000 cm^{-1} .

3.2. Electrostatic Potential (ESP) 2D Maps

By using ESP maps, it is possible to visualize the electron distribution, and therefore identify the centers or the areas of their concentration in each compound [63]. The contour maps of electron density reveal that oxygen atoms on the studied molecule inhibitors exhibit favorable interaction sites, taking into account the difference between the oxygen atoms in the functions and the other atom. The oxygen atoms, in this case, exist in the formyl group of FF1, in the formyl and hydroxyl groups of FF2 and in the hydroxyl and carboxylic groups in FF3. Interaction sites surrounded by a dark red contour contribute to form the bonding interactions between metal surfaces and inhibitors [13]. The dark red color in the contour map of negative potential particularly surrounds oxygen molecules and its regions in FF1, FF2 and FF3 molecules in gas and aqueous phases, whereas the green color is scattered in the positive potential region according to the contour representation of electrostatic at the DFT/B3LYP/6-31++G(2d,p) calculation level (Figure 4). Similar geometries were obtained in the aqueous phase (Figure 5).

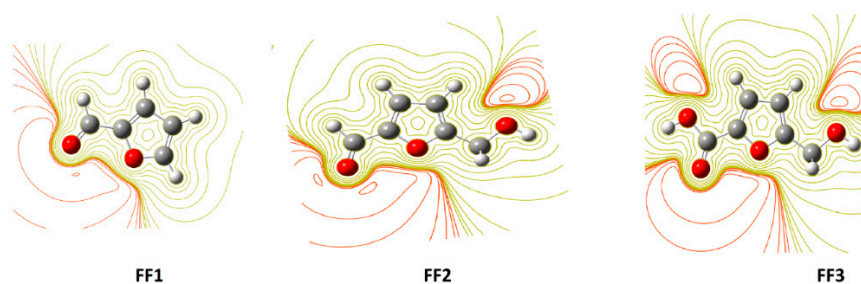


Figure 4. The contour representation of electrostatic potential regions of negative (positive) potential is red (green) for molecules in the gas phase using the DFT/B3LYP/6-31++G(2d,p) method.

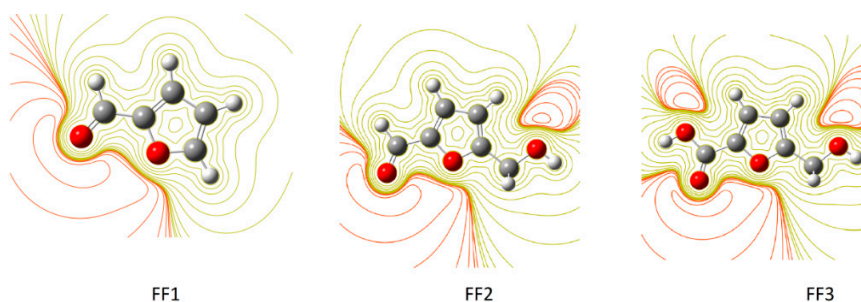


Figure 5. The contour representation of electrostatic potential regions of negative (positive) potential is red (green) for inhibitor molecules in aqueous phase using the DFT/B3LYP/6-31++G(2d,p) method.

3.3. HOMO and LUMO Energies and Derived Parameters

The highest occupied molecular orbital (HOMO) and the lowest unoccupied molecular orbital (LUMO) of a chemical molecule are very important in defining its reactivity [64,65]. Figures 6 and 7 represent the HOMO and LUMO orbitals of the studied compounds in gas and aqueous phases, respectively. The compounds FF1, FF2 and FF3 present a clear contribution of p -orbitals at the cyclical level (furan ring), consisting of an aromatic ring with five atoms, including one oxygen atom.

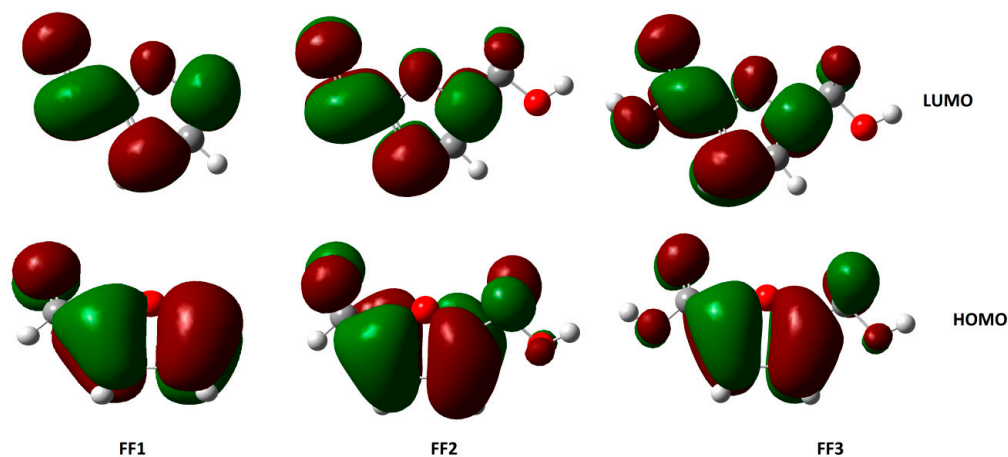


Figure 6. The highest occupied molecular orbitals (HOMOs) and lowest unoccupied molecular orbitals (LUMOs) of inhibitor molecules in gas phase using the DFT/B3LYP/6-31++G(2d,p) method.

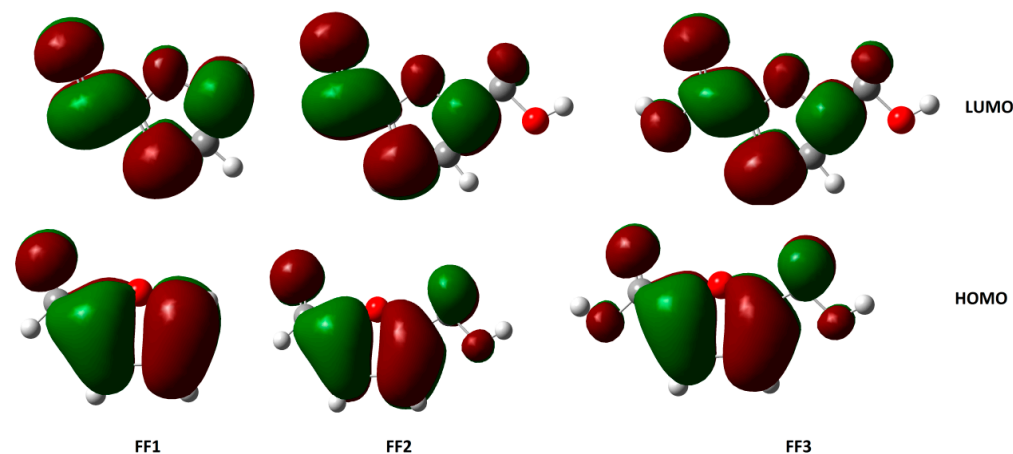


Figure 7. The HOMOs and LUMOs of inhibitor molecules in aqueous phase using the DFT/B3LYP/6-31++G(2d,p) method.

The quantum molecular results summarized in Tables 2 and 3 aims to describe in detail the energetic and structural characteristics of the studied molecules. The quantum chemical parameters calculated using the HF/6-31G++(2d,p), MP2/6-31G++(2d,p) and B3LYP/6-31G++(2d,p) methods for the inhibitors in aqueous and gas phases are E_{LUMO} , E_{HOMO} , ΔE , I , A , η , χ , ω , ε and ΔN . The E_{LUMO} and E_{HOMO} values are slightly different with a negligible difference for each method, which means that these are representative results. These two elements, E_{LUMO} and E_{HOMO} , are the basis for calculating all the other parameters that are estimated following the Koopmans theorem [66] to determine the properties related to the reactivity and selectivity of the inhibitor. Starting with the energy gap ΔE (i.e., $E_{HOMO} - E_{LUMO}$) is an essential parameter as the reactivity of the inhibitor compound, and thus an efficient inhibitor is characterized by a small energy gap [12]. All values of ΔE determined for the inhibitors studied by the different methods have the same order $FF1 > FF2 > FF3$, which shows that FF3 has good inhibitory power compared to the other inhibitors FF2 and FF1, respectively (Tables 1

and 2). Besides, the reactivity of the inhibitors can be also estimated by the other parameters, such as electronegativity expressed from E_{LUMO} and E_{HOMO} using Equation 2, depending on the results that show that FF3 has a small electronegativity value compared to FF2 and FF1. Therefore, concerning the reactivity of these compounds, FF3 tends more to react as a donor of electrons [14].

Table 2. Calculated quantum chemical parameters for the molecules in the gas phase (eV).

	ELUMO	EHOMO	ΔE	Energy	I	A	η	χ	ω	ε	ΔN
HF/6-31G++(2d,p)											
FF1	1.095	-9.673	10.768	-9284.422	9.673	-1.095	5.384	4.289	1.708	0.585	0.018
FF2	1.060	-9.322	10.382	-12,382.22	9.322	-1.060	5.191	4.131	1.643	0.608	0.034
FF3	1.031	-8.680	9.711	-23,703.52	8.680	-1.031	4.855	3.824	1.506	0.664	0.067
MP2/6-31G++(2d,p)											
FF1	0.976	-9.396	10.372	-9289.265	9.396	-0.976	5.186	4.210	1.709	0.585	0.026
FF2	0.950	-8.932	9.882	-12,388.66	8.932	-0.950	4.941	3.991	1.612	0.620	0.049
FF3	0.911	-8.513	9.423	-23,714.94	8.513	-0.910	4.712	3.801	1.533	0.652	0.072
B3LYP/6-31G++(2d,p)											
FF1	-1.751	-6.911	5.160	-9289.608	6.911	1.751	2.580	4.331	3.635	0.275	0.029
FF2	-1.649	-6.775	5.126	-12,389.13	6.775	1.649	2.563	4.212	3.461	0.289	0.052
FF3	-1.533	-6.638	5.104	-23,715.59	6.638	1.533	2.552	4.085	3.270	0.306	0.077

Table 3. Calculated quantum chemical parameters for the molecules in the aqueous phase (eV).

	ELUMO	EHOMO	ΔE	Energy	I	A	η	χ	ω	ε	ΔN
HF/6-31G++(2d,p)											
FF1	0.983	-8.952	9.935	-9343.37	8.952	-0.983	4.967	3.984	1.598	0.626	0.050
FF2	1.006	-8.857	9.863	-12,460	8.857	-1.006	4.932	3.925	1.562	0.640	0.056
FF3	1.031	-8.680	9.711	-23,861	8.680	-1.031	4.855	3.824	1.506	0.664	0.067
MP2/6-31G++(2d,p)											
FF1	0.868	-8.829	9.697	-9343.87	8.829	-0.868	4.848	3.980	1.634	0.612	0.051
FF2	0.886	-8.680	9.567	-12,460.8	8.681	-0.886	4.783	3.897	1.588	0.630	0.061
FF3	0.910	-8.513	9.423	-23,861.9	8.513	-0.910	4.712	3.801	1.533	0.652	0.072
B3LYP/6-31G++(2d,p)											
FF1	-1.704	-6.698	4.994	-9343.87	6.698	1.704	2.497	4.201	3.534	0.283	0.056
FF2	-1.852	-6.479	4.627	-12,460.8	6.479	1.852	2.314	4.165	3.749	0.267	0.068
FF3	-1.992	-6.210	4.217	-23,861.9	6.210	1.992	2.109	4.101	3.988	0.251	0.090

The global hardness (η) values were calculated using Equation 3, with softness values defined using Equation 3; after that, the global electrophilicity index (ω) were expressed in terms of the electronegativity and global hardness parameters according to Equation 3. All of these parameters are essential to deeply describe the reactivity of an inhibitor in addition to the ΔN as determined by Equation 4, which considers the most critical parameter because it combines several previous parameters; thus it gives a global description of the reactivity of an inhibitor. It is remarkable that the global hardness is listed in ascending order as following FF3, FF2 and FF1, and that means that FF3 is more reactive than both FF2 and FF1 (Table 3). This is because it is demonstrated that the chemical hardness of molecules is precisely the screened interaction energy of the electrons in the frontier (HOMO and LUMO) orbitals, which are the resistance of an atom to a charge transfer [67]. For the electrophilicity, which describes a good electrophile, while a small value of electrophilicity describes a good nucleophile that likes positive charges, the latter generally represent the charges of a metallic surface; therefore according to the obtained values, $FF3 > FF2 > FF1$ in this order react with a

positively charged metal surface. In addition to the number fraction of electrons transferred, ΔN for FF3, FF2 and FF1 are in agreement with all adopted bases, as reported in Table 3, which also confirms that FE3 has a high number of electron transfer, hence predicting that the FF3 has the highest inhibition performance compared to the other inhibitors FF2 and FF1. The number of transferred electrons (ΔN) gives information about the number of electrons transferred to the acceptor surface [68].

4. Charge Distribution

The presence of a high negative charge in some atoms or sites in compounds gives them a higher tendency to donate electrons to react with the metal surface. Knowing that, the reaction sites of the FF1, FF2 and FF3 molecules are the oxygen atoms, namely that of the molecular functions aldehyde ((H-C=O) and alcohol (-OH alcohol) or (-OH acid)). For this reason, one of the most common methods to present this property is Mulliken analysis [16]. The Mulliken partial charges on the different atoms of the optimized molecules studied are shown in Figures 8 and 9 and summarized in Table 4. These Mulliken charge distributions for the molecules are calculated at the B3LYP/6-31G++(2d,p) in the gas and aqueous phase. These distribution charges on some heteroatoms such as oxygen (O) and carbon (C) can make such groups into susceptible active centers, which explains the highest negative charges of some heteroatoms, especially the oxygen atom (O), because it is a part of inhibitors function groups. These groups part, react, or adsorb on a metallic surface.

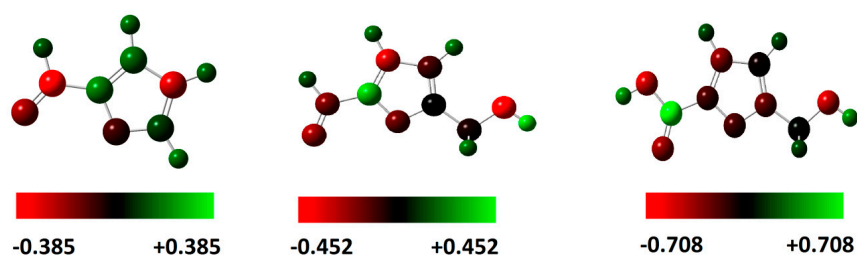


Figure 8. Mulliken charge distribution for the molecules calculated at the B3LYP/6-31G++(2d,p) in the gas phase.

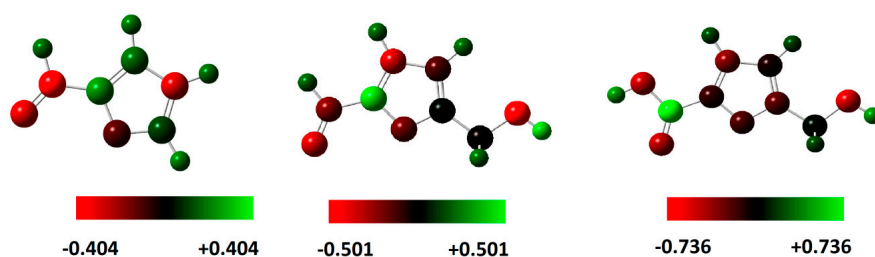


Figure 9. Mulliken charge distribution for the molecules calculated at the B3LYP/6-31G++(2d,p) in the aqueous phase.

Table 4. Mulliken charge distribution for the molecules calculated at the B3LYP/6-31G++(2d,p) in gas and aqueous phases.

	Atom	C1	C2	C3	C4	O5	C8	O9	C10	O13	O15
FF1	aq	0.001	-0.201	0.014	0.259	-0.170	-0.343	-0.296			
	gas	-0.003	-0.184	-0.014	0.257	-0.139	-0.331	-0.212			
FF2	aq	-0.020	-0.020	-0.440	0.434	-0.177	-0.182	-0.280	-0.098	-0.517	
	gas	-0.043	0.011	-0.418	0.383	-0.153	-0.151	-0.200	-0.128	-0.467	
FF3	aq	-0.125	0.042	-0.402	0.149	-0.212	0.597	-0.357	-0.075	-0.534	-0.551
	gas	-0.130	0.074	-0.386	0.110	-0.191	0.591	-0.296	-0.095	-0.486	-0.538

Furthermore, all negative atoms on the molecular skeleton can contribute to this process through an intramolecular synergistic effect [15].

5. Morphology of Studied Metal Surfaces

The obtained BFDH morphology results for selected metal substrates in the current study were summarized (Table 5). It can be seen that the multiplicities of Cu(111), Fe(110), Al(111) and Sn(111) faces are 8, 12, 8 and 8, respectively. This indicates that these faces have more contact sites to interact with furfural molecules. Furthermore, the larger d_{hkl} distances were obtained in the case of the Cu(111), Fe(110), Al(111) and Sn(111) faces, which reveals that these faces are densely packed metal surfaces. Furthermore, the higher % total facet area values are noted for the Cu(111), Fe(110), Al(111) and Sn(111) faces, which accounts for 78%, 64%, 78% and 100% of the crystal surface, respectively; this means there are the main faces where the adsorption process of furfural derivatives can occur. Accordingly, the (110), (110), (111) and (111) faces were chosen as representative surface models for copper, iron, aluminum and tin metal, respectively, during the Monte Carlo simulations.

Table 5. Bravais–Friedel–Donnay–Harker (BFDH) morphology results for selected metal substrates in this study.

Metal	(hkl)	Multiplicity	d_{hkl} (Å)	% Total Facet Area
Copper	(111)	8	2.1	78
	(200)	6	1.8	22
Iron	(110)	12	2.0	100
	(100)	6	1.4	64
Aluminum	(111)	8	2.3	25
	(200)	6	2.0	22
Tin	(111)	8	3.7	100
	(220)	12	2.3	0

6. Monte Carlo Simulations

The adsorption behaviors of FF1, FF2 and FF3 derivatives were conducted using Monte Carlo simulations on the Cu(111), Fe(110), Al(111) and Sn(111) surfaces. To perceive the equilibrium adsorption configuration of the studied molecules on the metals' surfaces, Figures 10–12 show how FF3, FF2 and FF1 could be adsorbed on the Fe(110), Cu(111), Al(111) and Sn(111) surfaces via two different views. From the side view, all inhibitor molecules are found to be parallel on the Fe(110), Cu(111) and Al(111) surfaces and quasi-parallel in the case of the Sn(111) surface. From the top view, all molecules are flat on the metal surfaces.

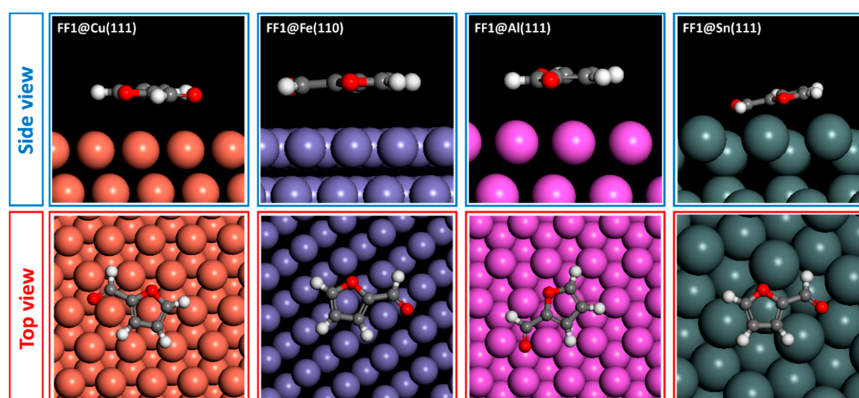


Figure 10. Adsorption configuration of FF1 compound on different metal surfaces.

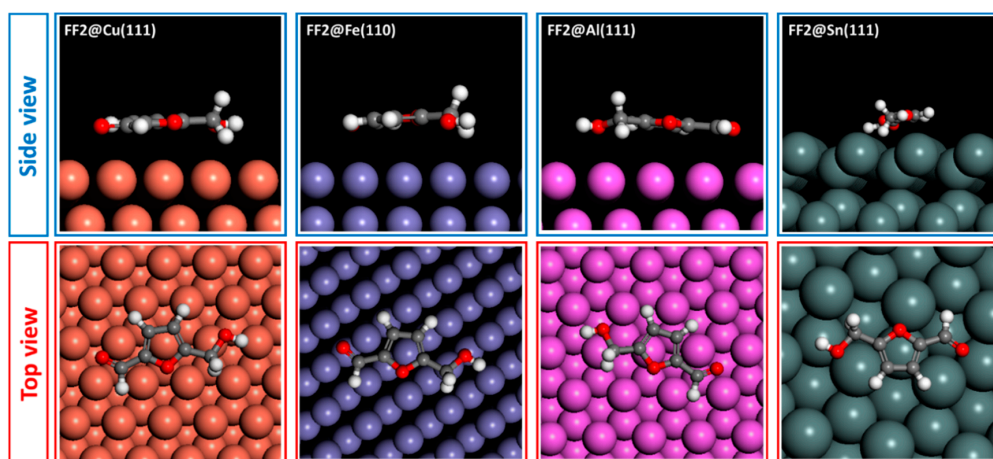


Figure 11. Adsorption configuration of FF2 compound on different metal surfaces.

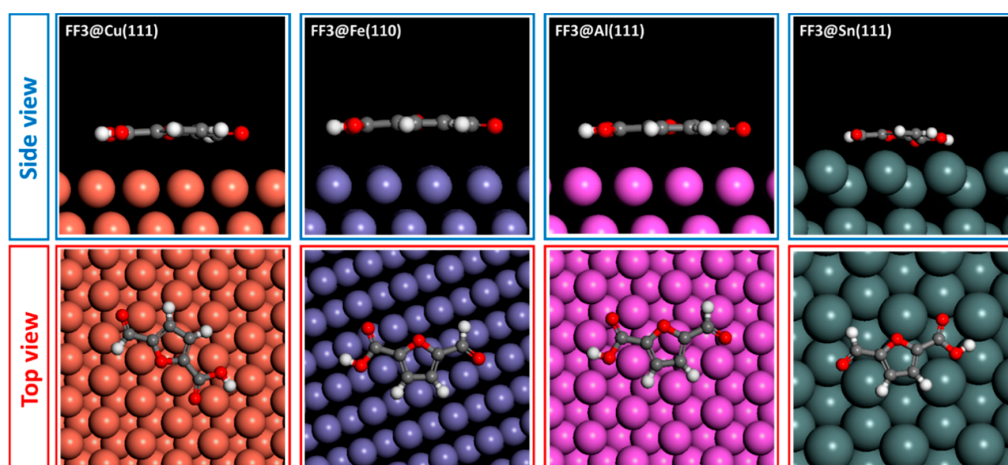


Figure 12. Adsorption configuration of FF3 compound on different metal surfaces.

The adsorption energies of all molecules are ordered as Fe(110) < Cu(111) < Al(111) < Sn(111) (Table 6). In the case of Fe(110), FF3 exhibits the lowest adsorption energy of $-77.539 \text{ kcal mol}^{-1}$. Hence, the adsorption energies increased from -71.963 to $-57.091 \text{ kcal mol}^{-1}$ for FF2 and FF1, respectively. The same order was observed in the case of Cu(111), Al(111) and Sn(111) surfaces. Indeed, the adsorption energies values on Cu(111) surface are -41.679 , -38.708 and $-30.689 \text{ kcal mol}^{-1}$ for FF3, FF2 and FF1, respectively. For the Al(111) surface, the values are -38.503 , -35.649 and $-28.414 \text{ kcal mol}^{-1}$ for FF3, FF2 and FF1, respectively. Finally, for the Sn(111) surface, the values are -30.138 , -28.179 and $-22.571 \text{ kcal mol}^{-1}$ for FF3, FF2 and FF1, respectively. Moreover, FF3 was found to be more stable and easily adsorbed on the studied surfaces. This conclusion could probably be explained by the existence of oxygen sites (O^9 , O^{13} and O^{15}) with negative charges of -0.628 , -0.745 and -0.683 , respectively. The negative charges (i.e., the red color regions) were clearly concentrated around the oxygen atoms with the order: $O^{13} > O^{15} > O^9$ (Figures 4 and 5).

Table 6. The adsorption energy of furfural derivatives (FF1, FF2 and FF3) and aggressive agents on the considered surfaces (in kcal mol^{-1}).

Metal Surface	Cu(111)	Fe(110)	Al(111)	Sn(111)
FF1	-30.689	-57.091	-28.414	-22.571
FF2	-38.708	-71.963	-35.649	-28.179
FF3	-41.679	-77.539	-38.503	-30.138

7. Conclusions

In summary, DFT calculation with different basis sets and Monte Carlo simulations were carried out to compare and evaluate the corrosion inhibition efficiencies of three furan derivatives, which are furan-2-carbaldehyde, 5-(hydroxymethyl) furfural and 5-(hydroxymethyl) furoic acid on Fe(110), Cu(111), Al(111) and Sn(111) surfaces. The theoretical vibrational study confirmed that all of these compounds are distinguished by the functional groups (aldehyde and carboxylic groups). The neutral and portioned forms were optimized and investigated. Using the results of DFT calculations, it was shown that FF3 has a small electronegativity value compared to FF2 and FF1. Therefore, concerning the reactivity of these compounds, FF3 has a larger tendency to react as a donor of electrons. Additionally, Monte Carlo simulations showed that the adsorption energies of all molecules are ordered as Fe(110) < Cu(111) < Al(111) < Sn(111). In conclusion, 5-(hydroxymethyl)furoic acid could be a good candidate for anticorrosive protection and should to be tested and studied, especially on iron surfaces in acidic media.

Author Contributions: H.B., B.B. and B.E.I. did the theoretical calculations; H.A.O., Y.A. and R.O. drafted the manuscript; S.E.I., M.H. and L.B. revised the manuscript; H.A.O., R.O. and C.L. planned and designed the whole study and finalized the manuscript. All authors have read and agreed to the published version of the manuscript.

Funding: This research received no external funding.

Conflicts of Interest: There are no conflicts to declare.

References

1. King, D.; Inderwildi, O.R.; Williams, A.; Hagan, A. The future of industrial biorefineries. In *Proceedings of the World Economic Forum White Paper*; World Economic Forum: Cologn/Geneva, Switzerland, 2010.
2. Koch, G.H.; Brongers, M.P.H.; Thompson, N.G.; Virmani, Y.P.; Payer, J.H. *Corrosion Cost and Preventive Strategies in the United States*; Federal Highway Administration: McLean, VA, USA, 2002.
3. Shaw, B.A.; Kelly, R.G. What is corrosion? *Electrochem. Soc. Interface* **2006**, *15*, 24–27.
4. Connatser, R.M.; Frith, M.G.; Jun, J.; Lewis Sr, S.A.; Brady, M.P.; Keiser, J.R. Approaches to investigate the role of chelation in the corrosivity of biomass-derived oils. *Biomass Bioenergy* **2020**, *133*, 105446. [[CrossRef](#)]
5. Hsissou, R.; Dagdag, O.; Abbout, S.; Benhiba, F.; Berradi, M.; El Bouchti, M.; Berisha, A.; Hajjaji, N.; Elharfi, A. Novel derivative epoxy resin TGETET as a corrosion inhibition of E24 carbon steel in 1.0 M HCl solution. Experimental and computational (DFT and MD simulations) methods. *J. Mol. Liq.* **2019**, *284*, 182–192. [[CrossRef](#)]
6. Dohare, P.; Quraishi, M.A.; Lgaz, H.; Salghi, R. Electrochemical DFT and MD simulation study of substituted imidazoles as novel corrosion inhibitors for mild steel. *Port. Electrochim. Acta* **2019**, *37*, 217–239. [[CrossRef](#)]
7. Bahlakeh, G.; Dehghani, A.; Ramezanzadeh, B.; Ramezanzadeh, M. Highly effective mild steel corrosion inhibition in 1 M HCl solution by novel green aqueous mustard seed extract: Experimental, electronic-scale DFT and atomic-scale MC/MD explorations. *J. Mol. Liq.* **2019**, *293*, 111559. [[CrossRef](#)]
8. El Ibrahimy, B.; El Mouaden, K.; Jmiai, A.; Baddouh, A.; El Issami, S.; Bazzi, L.; Hilali, M. Understanding the influence of solution's pH on the corrosion of tin in saline solution containing functional amino acids using electrochemical techniques and molecular modeling. *Surf. Interfaces* **2019**, *17*, 100343. [[CrossRef](#)]
9. Qiang, Y.; Zhang, S.; Tan, B.; Chen, S. Evaluation of Ginkgo leaf extract as an eco-friendly corrosion inhibitor of X70 steel in HCl solution. *Corros. Sci.* **2018**, *133*, 6–16. [[CrossRef](#)]
10. Motamedi, M.; Ramezanzadeh, B.; Mahdavian, M. Corrosion inhibition properties of a green hybrid pigment based on Pr-Urtica Dioica plant extract. *J. Ind. Eng. Chem.* **2018**, *66*, 116–125. [[CrossRef](#)]
11. Saxena, A.; Prasad, D.; Haldhar, R.; Singh, G.; Kumar, A. Use of *Sida cordifolia* extract as green corrosion inhibitor for mild steel in 0.5 M H₂SO₄. *J. Environ. Chem. Eng.* **2018**, *6*, 694–700. [[CrossRef](#)]
12. Ebenso, E.E.; Kabanda, M.M.; Arslan, T.; Saracoglu, M.; Kandemirli, F.; Murulana, L.C.; Singh, A.K.; Shukla, S.K.; Hammouti, B.; Khaled, K.F.; et al. Quantum chemical investigations on quinoline derivatives as effective corrosion inhibitors for mild steel in acidic medium. *Int. J. Electrochem. Sci.* **2012**, *7*, 5643–5676.
13. Iruthayaraj, A.; Chinnasamy, K.; Jha, K.K.; Munshi, P.; Pavan, M.S.; Kumaradhas, P. Topology of electron density and electrostatic potential of HIV reverse transcriptase inhibitor zidovudine from high resolution X-ray diffraction and charge density analysis. *J. Mol. Struct.* **2019**, *1180*, 683–697. [[CrossRef](#)]

14. Elusta, M.I.; Başaran, M.A.; Kandemirli, F. Theoretical studies on mild steel corrosion inhibition by 5-substituted 1H-tetrazoles in acidic media. *Int. J. Electrochem. Sci.* **2019**, *14*, 2743–2756. [[CrossRef](#)]
15. Oukhrib, R.; El Ibrahim, B.; Bourzi, H.; El Mouaden, K.; Jmiai, A.; El Issami, S.; Bammou, L.; Bazzi, L. Quantum chemical calculations and corrosion inhibition efficiency of biopolymer “chitosan” on copper surface in 3%NaCl. *J. Mater. Environ. Sci.* **2017**, *8*, 195–208.
16. Gao, G.; Liang, C. Electrochemical and DFT studies of β -amino-alcohols as corrosion inhibitors for brass. *Electrochim. Acta* **2007**, *52*, 4554–4559. [[CrossRef](#)]
17. Ahmed, S.K.; Ali, W.B.; Khadom, A.A. Synthesis and investigations of heterocyclic compounds as corrosion inhibitors for mild steel in hydrochloric acid. *Int. J. Ind. Chem.* **2019**, *10*, 159–173. [[CrossRef](#)]
18. Singh, A.; Ansari, K.R.; Quraishi, M.A.; Kaya, S.; Banerjee, P. The effect of an N-heterocyclic compound on corrosion inhibition of J55 steel in sweet corrosive medium. *New J. Chem.* **2019**, *43*, 6303–6313. [[CrossRef](#)]
19. Al Zoubi, W.; Ko, Y.G. Self-assembly of hierarchical N-heterocycles-inorganic materials into three-dimensional structure for superior corrosion protection. *Chem. Eng. J.* **2019**, *356*, 850–856. [[CrossRef](#)]
20. Benmahammed, I.; Douadi, T.; Issaadi, S.; Al-Noaimi, M.; Chafaa, S. Heterocyclic Schiff bases as corrosion inhibitors for carbon steel in 1 M HCl solution: Hydrodynamic and synergetic effect. *J. Dispersion Sci. Technol.* **2019**, 1–20. Available online: <https://doi.org/10.1080/01932691.2019.1614038> (accessed on 13 April 2020). [[CrossRef](#)]
21. Al-abdali, F.H.; Abdallah, M.; El-Sayed, R. Corrosion inhibition of aluminum using nonionic surfactant compounds with a six membered heterocyclic ring in 1.0 M HCl solution. *Int. J. Electrochem. Sci.* **2019**, *14*, 3509–3523. [[CrossRef](#)]
22. Verma, C.; Ebenso, E.E.; Quraishi, M.A. Alkaloids as green and environmental benign corrosion inhibitors: An overview. *Int. J. Corros. Scale Inhib.* **2019**, *8*, 512–528.
23. Cai, C.M.; Zhang, T.; Kumar, R.; Wyman, C.E. Integrated furfural production as a renewable fuel and chemical platform from lignocellulosic biomass. *J. Chem. Technol. Biotechnol.* **2014**, *89*, 2–10. [[CrossRef](#)]
24. Montané, D.; Salvadó, J.; Torras, C.; Farriol, X. High-temperature dilute-acid hydrolysis of olive stones for furfural production. *Biomass Bioenergy* **2002**, *22*, 295–304. [[CrossRef](#)]
25. Mansilla, H.D.; Baeza, J.; Urzua, S.; Maturana, G.; Villaseñor, J.; Durán, N. Acid-catalysed hydrolysis of rice hull: Evaluation of furfural production. *Bioresour. Technol.* **1998**, *66*, 189–193. [[CrossRef](#)]
26. Garcia-Olmo, A.J.; Yopez, A.; Balu, A.M.; Prinsen, P.; Garcia, A.; Maziere, A.; Len, C.; Luque, R. Activity of continuous flow synthesized Pd-based nanocatalysts in the flow hydroconversion of furfural. *Tetrahedron* **2017**, *73*, 5599–5604. [[CrossRef](#)]
27. Delbecq, F.; Wang, Y.; Muralidhara, A.; El Ouardi, K.; Marlair, G.; Len, C. Hydrolysis of hemicellulose and derivatives—A review of recent advances in the production of furfural. *Front. Chem.* **2018**, *6*, 146. [[CrossRef](#)] [[PubMed](#)]
28. Wang, Y.; Delbecq, F.; Kwapinski, W.; Len, C. Application of sulfonated carbon-based catalyst for the furfural production from d-xylose and xylan in a microwave-assisted biphasic reaction. *Mol. Catal.* **2017**, *438*, 167–172. [[CrossRef](#)]
29. Le Guenic, S.; Delbecq, F.; Ceballos, C.; Len, C. Microwave-assisted dehydration of D-xylose into furfural by diluted inexpensive inorganic salts solution in a biphasic system. *J. Mol. Catal. A Chem.* **2015**, *410*, 1–7. [[CrossRef](#)]
30. Delbecq, F.; Takahashi, Y.; Kondo, T.; Corbas, C.C.; Ramos, E.R.; Len, C. Microwave assisted efficient furfural production using nano-sized surface-sulfonated diamond powder. *Catal. Commun.* **2018**, *110*, 74–78. [[CrossRef](#)]
31. Delbecq, F.; Wang, Y.; Len, C. Conversion of xylose, xylan and rice husk into furfural via betaine and formic acid mixture as novel homogeneous catalyst in biphasic system by microwave-assisted dehydration. *J. Mol. Catal. A Chem.* **2016**, *423*, 520–525. [[CrossRef](#)]
32. Le Guenic, S.; Gergela, D.; Ceballos, C.; Delbecq, F.; Len, C. Furfural production from D-xylose and xylan by using stable Nafion NR50 and NaCl in a microwave-assisted biphasic reaction. *Molecules* **2016**, *21*, 1102. [[CrossRef](#)]
33. Obot, I.B.; Obi-Egbedi, N.O. Theoretical study of benzimidazole and its derivatives and their potential activity as corrosion inhibitors. *Corros. Sci.* **2010**, *52*, 657–660. [[CrossRef](#)]
34. Obot, I.B.; Obi-Egbedi, N.O.; Umoren, S.A. Antifungal drugs as corrosion inhibitors for aluminium in 0.1 M HCl. *Corros. Sci.* **2009**, *51*, 1868–1875. [[CrossRef](#)]

35. Kaya, S.; Kaya, C.; Guo, L.; Kandemirli, F.; Tüzün, B.; Uğurlu, İ.; Madkour, L.H.; Saraçoğlu, M. Quantum chemical and molecular dynamics simulation studies on inhibition performances of some thiazole and thiadiazole derivatives against corrosion of iron. *J. Mol. Liq.* **2016**, *219*, 497–504. [[CrossRef](#)]
36. Erdoğan, Ş.; Safi, Z.S.; Kaya, S.; Işın, D.Ö.; Guo, L.; Kaya, C. A computational study on corrosion inhibition performances of novel quinoline derivatives against the corrosion of iron. *J. Mol. Struct.* **2017**, *1134*, 751–761. [[CrossRef](#)]
37. El Belghiti, M.; Karzazi, Y.; Dafali, A.; Hammouti, B.; Bentiss, F.; Obot, I.B.; Bahadur, I.; Ebenso, E.E. Experimental, quantum chemical and *Monte Carlo* simulation studies of 3, 5-disubstituted-4-amino-1, 2, 4-triazoles as corrosion inhibitors on mild steel in acidic medium. *J. Mol. Liq.* **2016**, *218*, 281–293. [[CrossRef](#)]
38. Obot, I.B.; Kaya, S.; Kaya, C.; Tüzün, B. Density Functional Theory (DFT) modeling and *Monte Carlo* simulation assessment of inhibition performance of some carbohydrazide Schiff bases for steel corrosion. *Phys. E Low Dimens. Syst. Nanostruct.* **2016**, *80*, 82–90. [[CrossRef](#)]
39. Ledieu, A.; Devreux, F.; Barboux, P. *Monte Carlo* simulations of borosilicate glass corrosion: Predictions for morphology and kinetics. *J. Non Cryst. Solids* **2004**, *345*, 715–719. [[CrossRef](#)]
40. Verma, C.; Obot, I.B.; Bahadur, I.; Sherif, E.S.M.; Ebenso, E.E. Choline based ionic liquids as sustainable corrosion inhibitors on mild steel surface in acidic medium: Gravimetric, electrochemical, surface morphology, DFT and *Monte Carlo* simulation studies. *Appl. Surf. Sci.* **2018**, *457*, 134–149. [[CrossRef](#)]
41. Verma, C.; Lgaz, H.; Verma, D.K.; Ebenso, E.E.; Bahadur, I.; Quraishi, M.A. Molecular dynamics and *Monte Carlo* simulations as powerful tools for study of interfacial adsorption behavior of corrosion inhibitors in aqueous phase: A review. *J. Mol. Liq.* **2018**, *260*, 99–120. [[CrossRef](#)]
42. El Faydy, M.; Tourir, R.; Touhami, M.E.; Zarrouk, A.; Jama, C.; Lakhri, B.; Olasunkanmi, L.O.; Ebenso, E.E.; Bentiss, F. Corrosion inhibition performance of newly synthesized 5-alkoxymethyl-8-hydroxyquinoline derivatives for carbon steel in 1 M HCl solution: Experimental, DFT and *Monte Carlo* simulation studies. *Phys. Chem. Chem. Phys.* **2018**, *20*, 20167–20187. [[CrossRef](#)]
43. El Baciony, N.M.; Elgendy, A.; Nady, H.; Migahed, M.A.; Zaki, E.G. Adsorption characteristics and inhibition effect of two Schiff base compounds on corrosion of mild steel in 0.5 M HCl solution: Experimental, DFT studies, and *Monte Carlo* simulation. *RSC Adv.* **2019**, *9*, 10473–10485. [[CrossRef](#)]
44. Caley, F.; Velázquez, J.C.; Valor, A.; Hallen, J.M. Probability distribution of pitting corrosion depth and rate in underground pipelines: A *Monte Carlo* study. *Corros. Sci.* **2009**, *51*, 1925–1934. [[CrossRef](#)]
45. Khaled, K.F. *Monte Carlo* simulations of corrosion inhibition of mild steel in 0.5 M sulphuric acid by some green corrosion inhibitors. *J. Solid State Electrochem.* **2009**, *13*, 1743–1756. [[CrossRef](#)]
46. Dong, H.; Zheng, Y.; Hu, P. DFT study of furfural conversion on a Re/Pt bimetallic surface: Synergetic effect on the promotion of hydrodeoxygenation. *Phys. Chem. Chem. Phys.* **2019**, *21*, 8384–8393. [[CrossRef](#)] [[PubMed](#)]
47. Dong, H.; Zheng, Y.; Hu, P. A DFT study of direct furfural conversion to 2-methylfuran on the Ru/Co₃O₄ surface. *Phys. Chem. Chem. Phys.* **2019**, *21*, 1597–1605. [[CrossRef](#)]
48. Agrawal, N.; Gong, L.; Roman, A.; Mark, L.; Medlin, W.; Holewinski, A.; Janik, M.J. Mechanistic Investigations for Electrocatalytic Oxidation of Furfural Using Density Functional Theory. In Proceedings of the Meeting Abstracts; The Electrochemical Society: Pennington, NJ, USA, 2019; p. 1030.
49. Lin, Z.; Wan, W.; Yao, S.; Chen, J.G. Cobalt-modified molybdenum carbide as a selective catalyst for hydrodeoxygenation of furfural. *Appl. Catal. B* **2018**, *233*, 160–166. [[CrossRef](#)]
50. Wan, W.; Jiang, Z.; Chen, J.G. A Comparative study of hydrodeoxygenation of furfural Over Fe/Pt (111) and Fe/Mo 2 C surfaces. *Top. Catal.* **2018**, *61*, 439–445. [[CrossRef](#)]
51. Obot, I.B.; Macdonald, D.D.; Gasem, Z.M. Density functional theory (DFT) as a powerful tool for designing new organic corrosion inhibitors. Part 1: An overview. *Corros. Sci.* **2015**, *99*, 1–30. [[CrossRef](#)]
52. Kovačević, N.; Milošev, I.; Kokalj, A. The roles of mercapto, benzene, and methyl groups in the corrosion inhibition of imidazoles on copper: II. Inhibitor–copper bonding. *Corros. Sci.* **2015**, *98*, 457–470. [[CrossRef](#)]
53. El Ibrahim, B.; Jmiai, A.; El Mouaden, K.; Baddouh, A.; El Issami, S.; Bazzi, L.; Hilali, M. Effect of solution's pH and molecular structure of three linear α -amino acids on the corrosion of tin in salt solution: A combined experimental and theoretical approach. *J. Mol. Struct.* **2019**, *1196*, 105–118. [[CrossRef](#)]
54. Hölzl, J.; Schulte, F.K. Work function of metals. In *Solid Surface Physics*; Springer: Berlin, Germany, 1979; pp. 1–150.

55. Skriver, H.L.; Rosengaard, N.M. Surface energy and work function of elemental metals. *Phys. Rev. B* **1992**, *46*, 7157. [[CrossRef](#)] [[PubMed](#)]
56. Singh, A.; Ansari, K.R.; Quraishi, M.A.; Lin, Y. Investigation of corrosion inhibitors adsorption on metals using density functional theory and molecular dynamics simulation. In *Corrosion Inhibitors*; IntechOpen: London, UK, 2019.
57. Obot, I.B.; Haruna, K.; Saleh, T.A. Atomistic Simulation: A Unique and Powerful Computational Tool for Corrosion Inhibition Research. *Arab. J. Sci. Eng.* **2019**, *44*, 1–32. [[CrossRef](#)]
58. Kirkpatrick, S.; Gelatt, C.D.; Vecchi, M.P. Optimization by Simulated Annealing. *Science* **1983**, *220*, 671–680. [[CrossRef](#)] [[PubMed](#)]
59. Fabian, V. Simulated annealing simulated. *Computers Math. Applic.* **1997**, *33*, 81–94. [[CrossRef](#)]
60. Yang, L.; Dong, Y. Crystal morphology study of N, N'-diacetylchitobiose by molecular dynamics simulation. *Carbohydr. Res.* **2011**, *346*, 2457–2462. [[CrossRef](#)]
61. El Ibrahim, B.; Jmiai, A.; El Mouaden, K.; Oukhrib, R.; Soumou, A.; El Issami, S.; Bazzi, L. Theoretical evaluation of some α -amino acids for corrosion inhibition of copper in acidic medium: DFT calculations, Monte Carlo simulations and QSPR studies. *J. King Saud. Univ. Sci.* **2020**, *32*, 163–171. [[CrossRef](#)]
62. Kabanda, M.M.; Obot, I.B.; Ebenso, E.E. Computational Study of Some Amino Acid Derivatives as Potential Corrosion Inhibitors for Different Metal Surfaces and in Different Media. *Int. J. Electrochem. Sci.* **2013**, *8*, 10839–10850.
63. Albrecht, M.; Yi, H.; Köksal, O.; Raabe, G.; Pan, F.; Valkonen, A.; Rissanen, K. CF₃: An Electron-Withdrawing Substituent for Aromatic Anion Acceptors? “side-On” versus “on-Top” Binding of Halides. *Chem. Eur. J.* **2016**, *22*, 6956–6963. [[CrossRef](#)]
64. Fukui, K.; Yonezawa, T.; Shingu, H. A molecular orbital theory of reactivity in aromatic hydrocarbons. *J. Chem. Phys.* **1952**, *20*, 722–725. [[CrossRef](#)]
65. Wang, H.; Wang, X.; Wang, H.; Wang, L.; Liu, A. DFT study of new bipyrazole derivatives and their potential activity as corrosion inhibitors. *J. Mol. Model.* **2007**, *13*, 147–153. [[CrossRef](#)]
66. Stoyanova, A.E.; Peyerimhoff, S.D. On the relationship between corrosion inhibiting effect and molecular structure. *Electrochim. Acta* **2002**, *47*, 1365–1371. [[CrossRef](#)]
67. Senet, P. Chemical hardnesses of atoms and molecules from frontier orbitals. *Chem. Phys. Lett.* **1997**, *275*, 527–532. [[CrossRef](#)]
68. Salman, T.A.; Zinad, D.S.; Jaber, S.H.; Al-Ghezi, M.; Mahal, A.; Takriff, M.S.; Al-Amiery, A.A. Effect of 1,3,4-thiadiazole scaffold on the corrosion inhibition of mild steel in acidic medium: An experimental and computational study. *J. Bio. Tribo. Corros.* **2019**, *5*, 1–11. [[CrossRef](#)]



© 2020 by the authors. Licensee MDPI, Basel, Switzerland. This article is an open access article distributed under the terms and conditions of the Creative Commons Attribution (CC BY) license (<http://creativecommons.org/licenses/by/4.0/>).